Process monitoring of directed-energy deposition of Inconel-718 via plume imaging

A. R. Nassar*, Brandon Starr*, and E. W. Reutzel*

* Applied Research Laboratory at the Pennsylvania State University,

University Park, PA 16802

Abstract

Laser-metal interactions typically results in vaporization and plume formation. These phenomena are complex and depend upon the details of the laser-vapor-melt interactions. As such, plume characteristics are sensitive to changes in process characteristics. Here, a spectroscopy-based imaging technique is presented for the monitoring of directed energy deposition of Inconel 718. Plume geometry is shown to be related to the processing parameters and geometry of single-bead deposits.

1. Introduction

Many strategies have been used to monitor additive manufacturing (AM)processes [1]–[3]. Some of these strategies include monitoring melt pool geometry [4]–[10] or temperature [9], [11], [12]. Another, less-studied strategy is the use of optical emission spectroscopy (OES) for monitoring AM builds [13]–[16].

OES is a good candidate for monitoring of AM processes given the sensitivity of optical emissions to system variables and process anomalies. Bartkowaik [13] has shown that the intensity of Cr line emissions vary with laser power or scan speed during DED of the Ni-Cr alloy Inconel® 625. Recent work [14] has also demonstrated that the line-to-continuum ratio of certain spectral emissions during DED of ASTM grade 5 titanium (Ti-6Al-4V) could be used to monitor and detect lack-of-fusion defects. Pekkarinen et al. [17] have also observed, though camera monitoring of the melt pool and vapor plume formed during DED of an austenitic, nickel-chromium stainless steel powder (Metco 41C), that the vapor plume can be used to characterize the process stability and indicate the degree of dilution within a melt pool. Though plume monitoring appeared to be coincidental in their work [17], conditions were identified at which the vapor plume emitted from the evaporating melt surface acted as a barrier that prevented powder from entering the melt pool. Similar effects have previously been identified for laser nitriding [18].

Work in the field of laser cladding has also demonstrated that plume emissions are indicative of clad quality [19], [20]. For instance, Tewari [19] showed that the intensities and ratios of certain Nb, Hf, and Al lines could be directly related to clad thickness. More recently, Ya et al.[20], showed that conditions at which powder melted and bonded to the substrate during DED of an austenitic, nickel-chromium stainless steel powder (Metco 42C), could be identified using the ratio of two iron absorption lines.

Tewari [19] also showed that the spectral line intensities correlated with the concentration of alloying elements of the deposited material. Separate works by Song and Mazumder [16] and Bartkowiak [13] also showed that optical emissions could be used to measure alloying element concentrations during DED. Song et al., [15] further claim that phase transformation during DED of a Ni-Ti, Ni-Al, and a Ti-Fe alloys are identifiable using a line-ratio technique.

Here, experiments are described wherein key DED process variables—laser power, translation speed, and working distance—are dynamically varied and related to plume geometry. Additionally, geometries of the resulting deposited tracks are also related to observed plume geometries. It is demonstrated that emitted plume geometry is closely related to processing variables as well as the resulting track geometries.

2. Experimental Setup

A directed-energy deposition, laser-based, Optomec, Inc. LENS MR-7 system was used to deposit Inconel® alloy 718 powder atop 3.175 mm (0.25 in) thick Inconel® alloy 718 substrates—see Table 1 for elemental composition [21]. During deposition, 6.5 grams/minute of powder was directed by four, radially-symmetrically-oriented nozzles. The substrate was positioned at a working distance measured between the substrate and exit of the powder nozzles.

Table 1. Minimum and Maximum Percentages of Elements Comprising Inconel® alloy 718 [21].

Ni (+Co)	Cr	Fe	Ni (+Ta)	Mo	Ti	Al	Co	C	Mn	Si	P	S	B	Cu
50.00	17.00	Bal.	4.75	2.80	0.65	0.20	—	—	—	—	—	—	—	—
55.00	21.00		5.50	3.30	1.15	0.80	1.00	0.08	0.35	0.35	0.015	0.015	0.006	0.30

An ytterbium-doped fiber laser with a maximum output power of 500 W was for deposition. Processing was conducted within an argon environment containing less than 20 ppm oxygen. A two-axis stage was used to translate the substrate in the x-y plane while a one-axis stage translated the deposition head in the vertical, build-up direction.

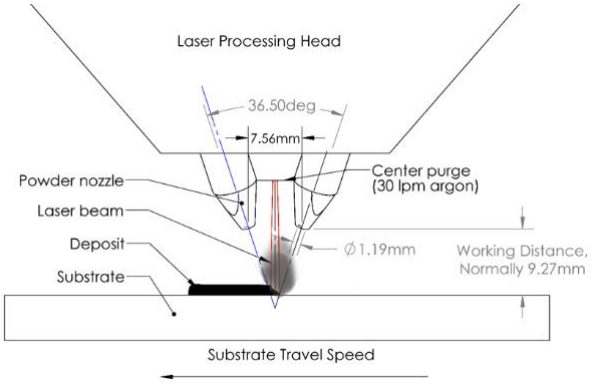

Figure 1: Deposition arrangement with plume shown emitting from laser-powder-substrate interaction region.

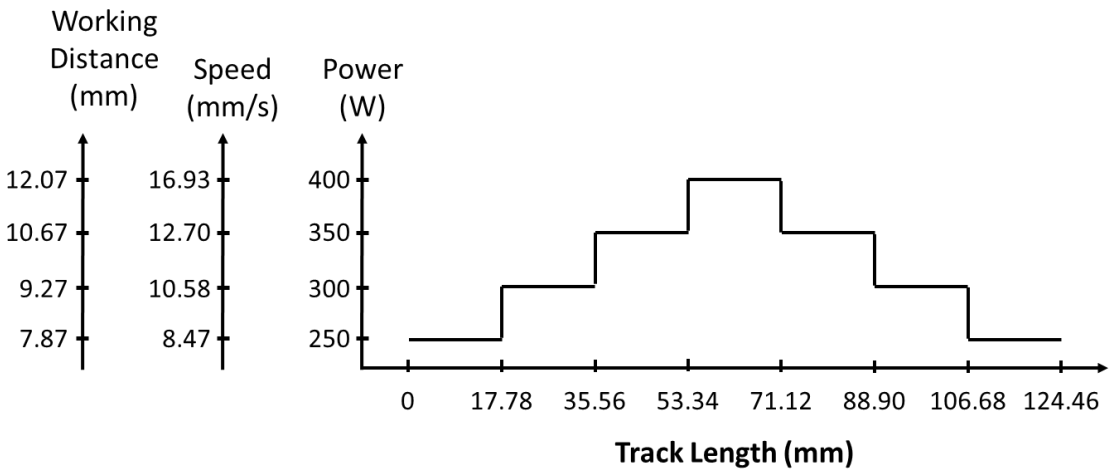

Figure 2: Variation of process variable with track length. For each experiment, one parameter, denoted by an ordinate axis, was varied dynamically, with all others constant.

Single-track deposits were performed wherein three processing parameters were varied: laser power, working distance and linear travel speed. For each experiment, one parameter was varied dynamically, with all others constant. Nominal processing parameters, two of which remained constant during each experiment, were a working distance of 9.27 mm, a translation speed of 10.58 mm/s, and a laser power of 350 W (measured at the substrate). The variable parameter was varied along the length of a track as shown in Figure 2.

The plume emitted from the laser-powder-melt interaction zone was imaged using a Basler Pilot piA640-210gm CCD camera oriented approximately parallel to the substrate and 45 degrees from the travel direction. The camera captured images at 13 frames per second and was equipped with custom imaging optics and a 430 nm (10 nm FWHM) band-pass filter. Within the FWHM of the band-pass filter, several strong iron atomic emission lines (Fe I) were expected [22], along with continuum emissions from the plume.

(a) (b)

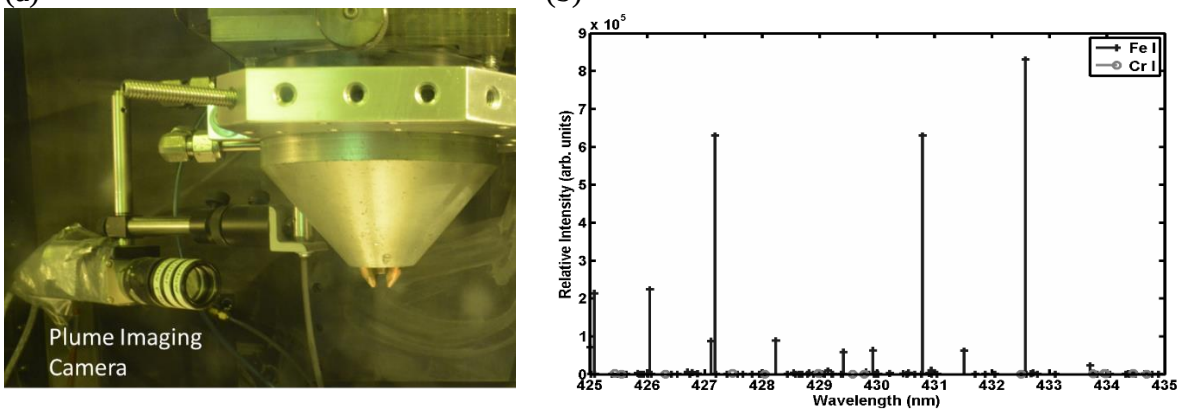

Figure 3: (a) CCD camera alignment relative to laser processing head. The substrate travel direction is into page. (b) Ni I, Cr I, and Fe I spectral emissions within the FWHM of the 430 nm band-pass filter.

Captured plume images were processed and analyzed in several steps. Using a calibration grid oriented parallel to the build-up direction and 45 degrees from the substrate-travel direction, a projective transformation was applied. This transformation is illustrated in Figure 4. After transformation, a threshold was applied to a produce a binary image. Next, a contiguous search algorithm, starting with the location of the brightest pixel in the frame, was applied to find all connected bright pixels—the defined region constituted the plume. Calculated plume metrics, including plume width and height defined using a bounding box. Plume area and plume centroid were also recorded along with the maximum plume (grayscale) intensity, prior to binarization of the image.

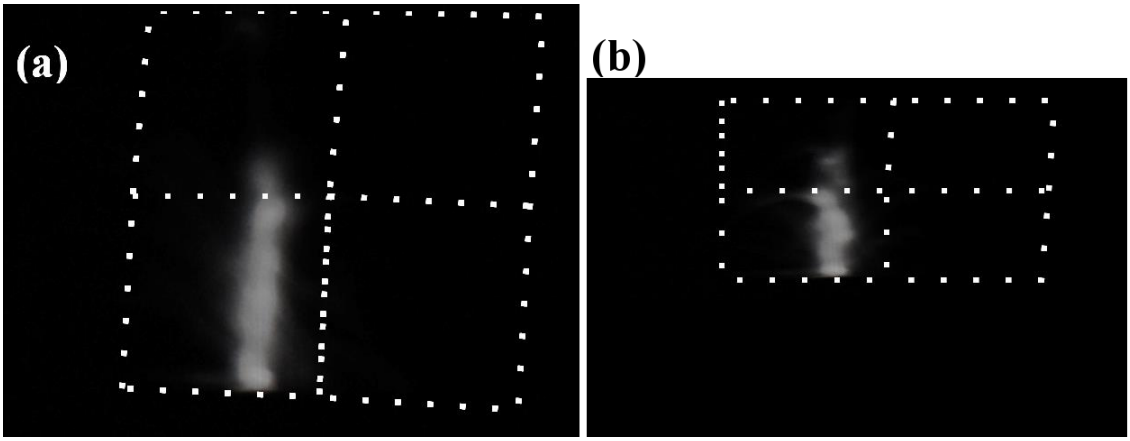

Figure 4: (a) Captured plume image. (b) Transformed plume image. Dashed, while lines show a calibration grid (each square of which is 5.08 x 5.08 mm) used for calibration.

The surface topology of deposited tracks were characterized using a Zygo NewView 8000 series optical profilometer. An example of captured profilometery data and analysis are shown in Figure 3. Track topology was measured with a lateral resolution less than 6 μm and a height resolution of less than 1 μm. At each measured position along the length of the deposit, the bead width, height, and contract angle were measured using a width-detection, and height-fitting algorithm with noise filtering based on a best-fit second-degree polynomial.

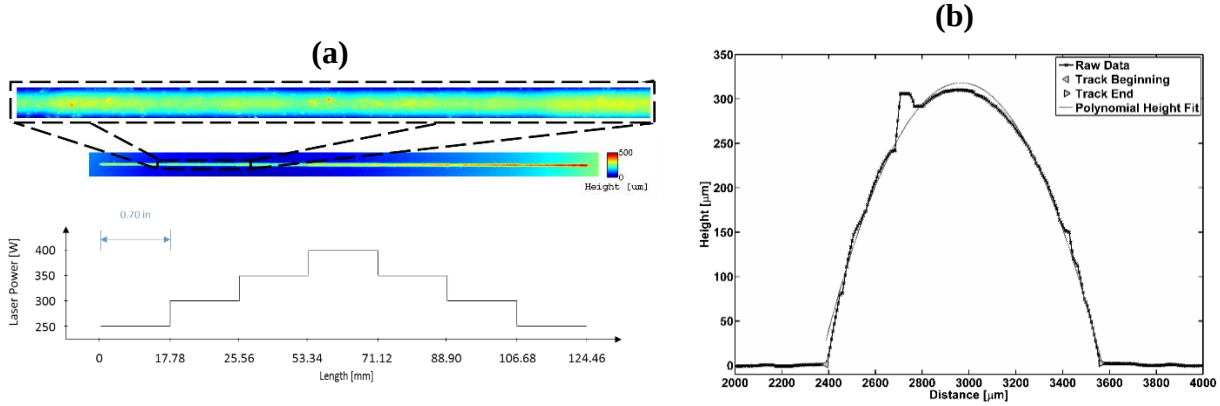

Figure 5: (a) Sample profilometry data shown together with the laser-power variation along the length of the deposited track. (b) Illustration of data analysis for determination of width, height and contract angle.

3. Results and Data Analysis

Plume metrics, including height, width, area, and maximum intensity were analyzed to determine if a relationship between processing parameters, plume metrics, and the resulting track geometry existed. In this section, single-track heights and widths are juxtaposed with measured plume height and width. Additionally, the maximum intensity and plume area are compared with track geometry.

Though the raw data show evidence of measurement noise, the single-track deposit in which laser power was varied along the track length (see Figure 6) indicate a clear relationship between laser power, track width, and plume geometry. As shown in Figure 6, both track height and width were affected by power variation, with the tallest and widest track geometry existing at the track length where power was maximum. Track width was more strongly impacted by variation in laser power than was track height, e.g. an 80% increase in laser power resulted in an approximately 33% increase in track width but only a 15% increase in track height. Measured plume width and height were also affected by variations in laser power and appeared to relate to deposit geometry, e.g. plume width increased approximately 45% and plume height increased approximate 63% with an 80% increase in laser power.

In addition to plume width and height, the integrated plume area and its maximum intensity were analyzed. As shown in Figure 7, variation in laser power impacted the maximum plume intensity as well as the plume area. Dynamic transitions in the maximum intensity, along the length of the track, coincide with concomitant transitions in laser power and track geometry.

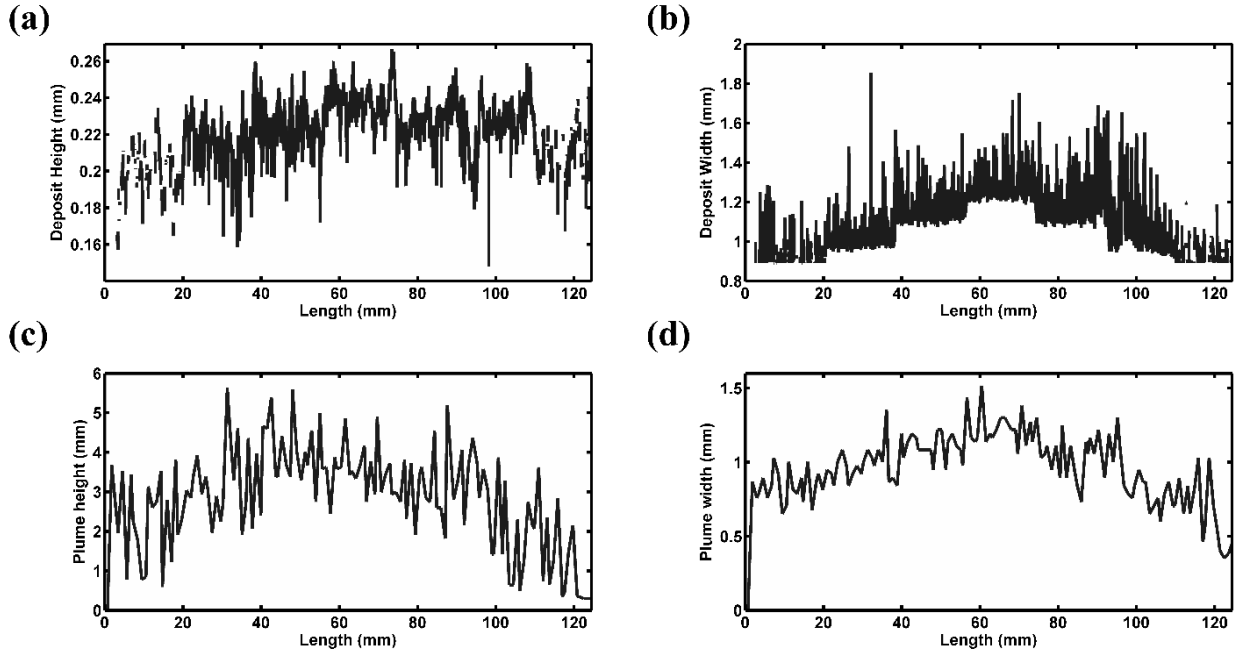

Figure 6: Track and plume characteristic resulting from variation of laser power. (a) Deposited track height and (b) Deposited track width measured using optical profilometry. (c) Plume height and (d) plume width measured using in-process CCD imaging.

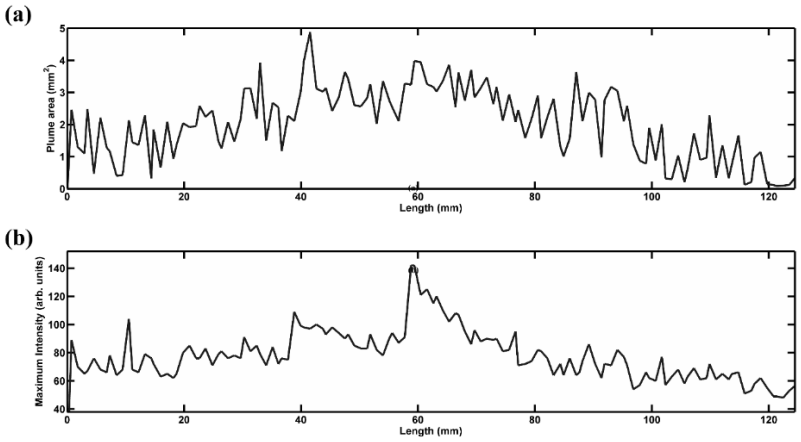

Figure 7: (a) Plume area and (b) maximum intensity resulting from variation of laser power

Compared with variation of laser power, variation of translation speed had a more pronounced effect on track height and a less pronounced effect on track width. As shown in Figure 8, a 100% increase in translation speed resulted in an approximately 60% decrease in track height and 13% decrease in track width. Qualitatively, plume height appeared to be affected by an increase in travel speed during the first half of the track, but remained constant during the decrease in translation speed in the second half of the track. Plume width also appeared to be more strongly affected by an increase in speed in the second half than by a decrease in speed in the second half.

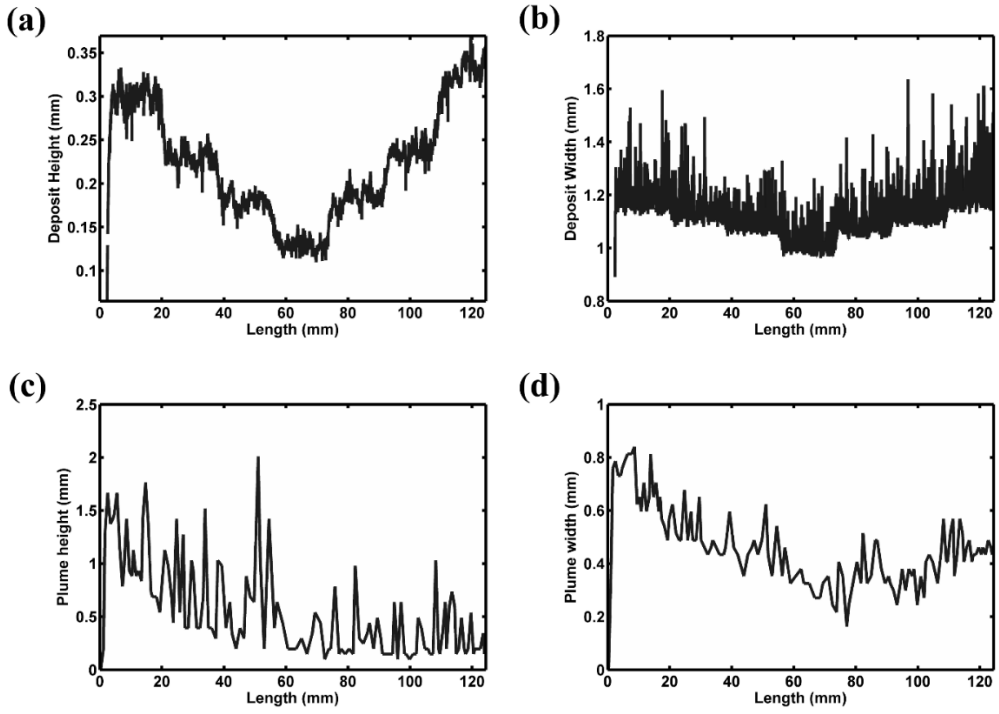

Figure 8: Track and plume characteristic resulting from variation of translation speed. (a) Deposited track height and (b) Deposited track width measured using optical profilometry. (c) Plume height and (d) plume width measured using in-process CCD imaging.

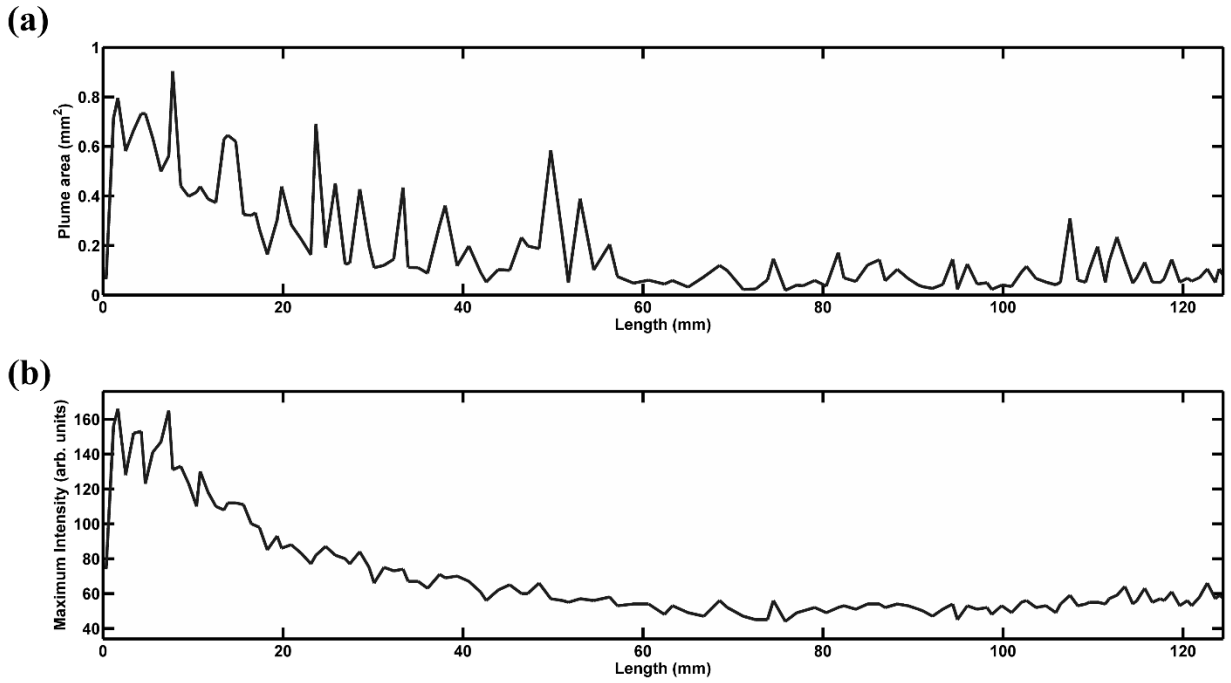

Figure 9: (a) Plume area and (b) maximum intensity resulting from variation of translation speed.

Plume area and maximum intensity, shown in Figure 9, varied similarly to plume height. Area and maximum intensity were highest at the start of the processed track, decreased to their lowest values mid-way through the track, and increased but did not approach the start-value during the second half of the track. The reasons for this non-intuitive result are unclear, and warrant further investigation.

Variations in working distance had a pronounced effect on track height but little effect on track width. As shown in Figure 10, plume height was also more affected by the variation in working distance than plume width. It should be noted that at the center of the track, from 53.34 to 71.12 mm, plume images were incomplete—a portion of the plume was below the imaging area. Plume measurement at the central portion of the deposited track should be disregarded. An increase in working distance from 7.87 to 10.67 mm (~36%) resulted in an increase in track height from 0.08 mm to 0.3 mm (275%) and a decrease in plume height from approximately 5 mm to 2 mm (60 %). The decrease in plume height with an increase in track height is opposite to what was observed in Figure 6 and Figure 8, and may serve as data to enable differentiation of the various process conditions.

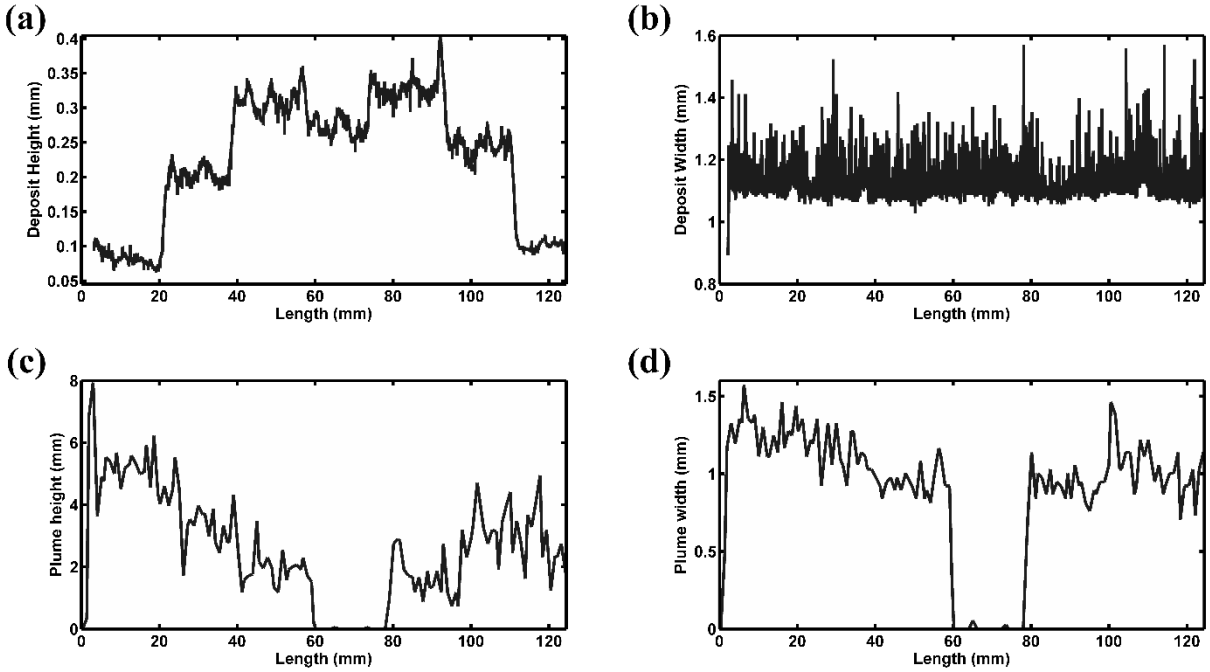

Figure 10: Track and plume characteristic resulting from variation of working distance. (a) Deposited track height and (b) Deposited track height measured using optical profiliometry. (c) Plume height and (d) plume width measured using in-process CCD imaging.

A decrease in plume area and maximum intensity was also observed with increasing working distance. Here too, plume measurement at the track center should be disregarded due to an incomplete image. Regions with varying working distances are clear in plume area measurements.

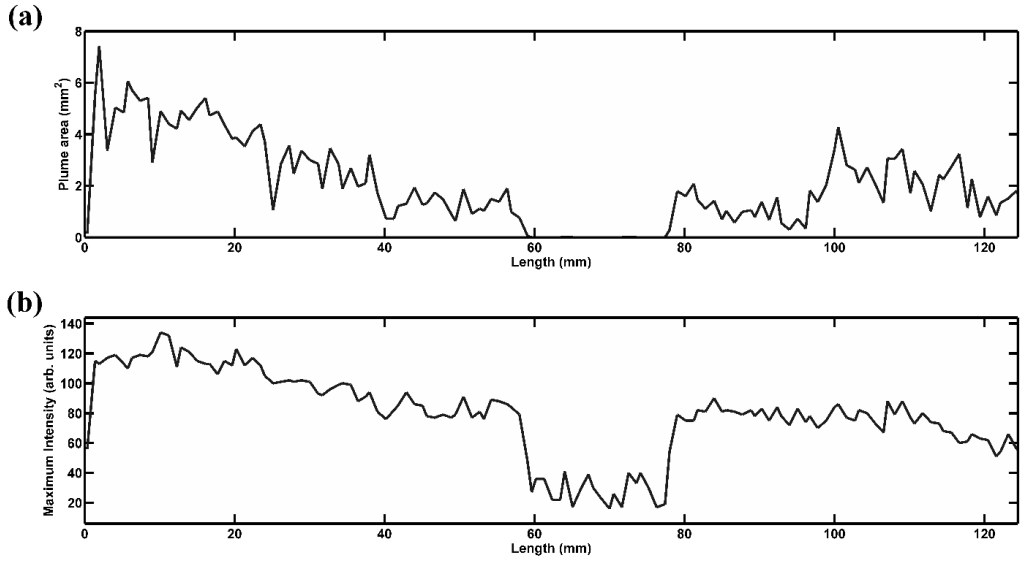

Figure 11: (a) Plume area and (b) maximum intensity resulting from variation of working distance.

4. Discussion

The results presented here show that plume geometry and intensity can be related to processing conditions and resulting track geometry. Maximum plume intensity varied directly with variations in laser power as did plume area, height, and width. Relationships between plume height, area and intensity and variations in processing speed were more difficult to discern, though the variation in plume width appeared to relate more strongly to variations in speed than to other metrics. Plume geometry and intensity were also directly affected by variation in working distance.

Both plume and track geometry measurements contained substantial fluctuation. Fluctuations in track geometry (Figure 6(a) and (b)) result from measurement and analysis noise as well as partially-sintered powder particles—the mean powder particle diameter was 120 μm—adhering to the surface of the deposit. Analysis of fluctuations in plume geometry was confounded by the low frame capture rate along with the rapid hydrodynamic fluctuations of the plume.

In all cases, plume width appeared to be closely related to the deposited track width. This ought not to be surprising given that the plume results from vaporization of the melt front. Given that the width of melt front defines the width of the melt pool, the width of the vapor plume ought to be closely related to the width of the underlying melt pool.

Plume height also showed variation with processing parameters in all cases, though its relationship to deposited track height is unclear. An increase in deposited track height, resulting from an increase in laser power or a reduction in translation speed, resulted in an increase in plume height. However, an increase in track height resulting from an increase in working distance resulted in a decrease in plume height along with plume area and intensity.

One explanation for the reduction in plume height, intensity, and area with increasing working distance may relate to the laser focusing geometry. At all working distances, the waist of the laser beam was above the substrate. Thus the focal point moved away from the substrate and the laser spot size at the substrate increased with increasing working distance. Given that the melt pool temperature and evaporation rate are related to the laser beam intensity at the surface, as the laser spot size increases with increasing working distance the evaporation rate and temperature of the vapor exiting the melt pool are expected to decrease. One should however be cautious in attempting to quantify this effect due to complex laser-plume-melt interactions, changes in the powder focusing geometry with working distance, along with the knowledge that the laser intensity profile may vary (e.g. for a top-hat beam distribution at focus) with distance from the focal point.

5. Concluding Remarks

Monitoring of metal additive manufacturing processes via examination of plume emissions appears to be a viable technique. Plume geometry and intensity have been shown here to be sensitive to processing parameters and deposited geometry.

Additional work is required to determine the precise, multi-dimensional relationship between plume metrics and processing conditions. This includes refined experiments with higher sampling rates, the examination of additional spectral ranges, extension to multi-track and multi-layer deposits, and consideration of parameter interactions. Further work along these lines and to statistically-relate plume metrics to process variations and resulting deposition geometries is underway.

A primary takeaway from this work is that processing conditions and resulting deposition geometries may be assessed via monitoring of plume emissions. Given that the presence of a plume may obstruct direct imaging or measurement of melt pool geometry and temperature, sensing plume emissions may be an alternative, and possible a preferred, means of monitoring and control of directed energy deposition processes. Similar conclusions, based on preliminary work, are expected for powder-bed deposition processes.

Acknowledgements

This work was supported by the Office of Naval Research, under Contract No. N00014-11-1-0668. Any opinions, findings and conclusions or recommendations expressed in this publication are those of the authors and do not necessarily reflect the views of the Office of Naval Research.

References

[1] E. W. Reutzel and A. R. Nassar, "A survey of sensing and control systems for machine and process monitoring of directed-energy, metal-based additive manufacturing," *Rapid Prototyp. J.*, vol. 21, no. 2, pp. 159–167, Mar. 2015.

[2] B. K. Foster, E. W. Reutzel, A. R. Nassar, C. J. Dickman, and B. T. Hall, "A brief survey of sensing for additive manufacturing," in *SPIE DSS 2015 - Defense, Security and Sensing*, Baltimore, Maryland, 2015.

[3] M. R. Boddu, R. G. Landers, and F. W. Liou, "Control of laser cladding for rapid prototyping—A review," in *Solid Freeform Fabrication Symposium Proceedings, University of Texas, Austin, TX*, 2001, pp. 6–8.

[4] J. R. Araujo, J. J. Rodriguez-Andina, J. Farina, F. Vidal, J. L. Mato, and M. A. Montealegre, "FPGA-based laser cladding system with increased robustness to optical defects," in *IECON 2012-38th Annual Conference on IEEE Industrial Electronics Society*, Montreal, QC, 2012, pp. 4688–4693.

[5] G. Bi, B. Schürmann, A. Gasser, K. Wissenbach, and R. Poprawe, "Development and qualification of a novel laser-cladding head with integrated sensors," *Int. J. Mach. Tools Manuf.*, vol. 47, no. 3–4, pp. 555–561, Mar. 2007.

[6] A. Heralić, A.-K. Christiansson, M. Ottosson, and B. Lennartson, "Increased stability in laser metal wire deposition through feedback from optical measurements," *Opt. Lasers Eng.*, vol. 48, no. 4, pp. 478–485, Apr. 2010.

[7] J. T. Hofman, B. Pathiraj, J. van Dijk, D. F. de Lange, and J. Meijer, "A camera based feedback control strategy for the laser cladding process," *J. Mater. Process. Technol.*, vol. 212, no. 11, pp. 2455–2462, Nov. 2012.

[8] D. Hu, H. Mei, and R. Kovacevic, “Closed loop control of 3D laser cladding based on infrared sensing,” in *Solid Freeform Fabrication Symposium Proceedings, University of Texas, Austin, TX*, 2001, pp. 129–137.
[9] D. A. Kriczky, J. Irwin, E. W. Reutzel, P. Michaleris, A. R. Nassar, and J. Craig, “3D spatial reconstruction of thermal characteristics in directed energy deposition through optical thermal imaging,” *J. Mater. Process. Technol.*, vol. 221, pp. 172–186, Jul. 2015.
[10] J.-P. Kruth, P. Mercelis, J. Van Vaerenbergh, and T. Craeghs, “Feedback control of selective laser melting,” in *Proceedings of the 3rd International Conference on Advanced Research in Virtual and Rapid Prototyping*, Leiria, Portugal, 2007, pp. 521–527.
[11] G. Bi, A. Gasser, K. Wissenbach, A. Drenker, and R. Poprawe, “Identification and qualification of temperature signal for monitoring and control in laser cladding,” *Opt. Lasers Eng.*, vol. 44, no. 12, pp. 1348–1359, Dec. 2006.
[12] L. Song and J. Mazumder, “Feedback control of melt pool temperature during laser cladding process,” *Control Syst. Technol. IEEE Trans. On*, vol. 19, no. 6, pp. 1349–1356, 2011.
[13] K. Bartkowiak, “Direct laser deposition process within spectrographic analysis in situ,” *Phys. Procedia*, vol. 5, pp. 623–629, Jan. 2010.
[14] A. R. Nassar, T. J. Spurgeon, and E. W. Reutzel, “Sensing defects during directed-energy additive manufacturing of metal parts using optical emissions spectroscopy,” in *Solid Freeform Fabrication Symposium Proceedings, University of Texas, Austin, TX*, 2014.
[15] L. Song, C. Wang, and J. Mazumder, “Identification of phase transformation using optical emission spectroscopy for direct metal deposition process,” 2012, p. 82390G–82390G–9.
[16] L. Song and J. Mazumder, “Real Time Cr Measurement Using Optical Emission Spectroscopy During Direct Metal Deposition Process,” *IEEE Sens. J.*, vol. 12, no. 5, pp. 958–964, May 2012.
[17] J. Pekkarinen, A. Salminen, and V. Kujanpää, “Laser cladding with scanning optics: Effect of scanning frequency and laser beam power density on cladding process,” *J. Laser Appl.*, vol. 26, no. 3, p. 032002, Aug. 2014.
[18] A. R. Nassar, “Investigation of laser-sustained plasma and the role of plasma in carbon dioxide laser nitriding of titanium,” The Pennsylvania State University, University Park, PA, 2012.
[19] S. K. Tewari, “Plasma optical emission spectroscopy of laser cladding for process control and oxidation behavior of laser clad NbAl alloys,” University of Illinois at Urbana-Champaign, Urbana, Illinois, 1995.
[20] W. Ya, A. R. Konuk, R. Aarts, B. Pathiraj, and B. Huis in ‘t Veld, “Spectroscopic monitoring of metallic bonding in laser metal deposition,” *J. Mater. Process. Technol.*, vol. 220, pp. 276–284, Jun. 2015.
[21] Special Metals Corporation, “INCONEL alloy 718,” SMC-045, Sep. 2007.
[22] A. Kramida, Y. Ralchenko, and J. Reader, NIST ASD Team, *NIST Atomic Spectra Database*. Gaithersburg, MD: National Institute of Standards and Technology, 2015.